29

Aero - Optics: Controlling Light with Air

Cosmas Mafusire[1,2] and Andrew Forbes[1,2]
[1]*Council for Industrial Research National Laser Centre*
[2]*School of Physics, University of KwaZulu-Natal*
South Africa

1. Introduction

It is possible to control light in a medium comprising nothing more than a fluid, whether in gas or liquid phase. Using air as an example, it is possible to bend light by a process of continuous refraction as opposed to stepwise refraction in the case of solid state optics. This is achieved by effecting a continuous change of the refractive index from a high value for lowest temperature (or high density) to a low value for the highest temperature (or lowest density). Since the density changes gradually from a low to a high value, the refractive index is graded as well. In fact, this effect is well known in nature: the mirage effect where light refracts away from a hot surface, usually a road or desert sand, is precisely due to continuous refraction of light. If the refractive index can be customised and controlled, then one has the possibility to create aero-optics: control of light with air. Such optics are a special subset of GRIN (Graded Refractive INdex) optics, with the most studied example being the simple lens, so-called gas lenses. The efficiency at which these lenses operate is dependent on the effectiveness of the refractive index gradient – the greater the gradient, the stronger the lens. There are advantages to such optics: they are not dispersive, and hence suitable for broad bandwidth laser pulses, and have no practical damage threshold as compared to most solid-state optics (e.g., glass). This latter point remains to be exploited for high power laser beam delivery in such applications as laser fusion and peta-watt high intensity laser beam delivery.
In the remainder of this chapter we will consider such gas lenses in more detail. We outline a simple approach to controlling light through a medium comprising nothing more than air in a spinning pipe that is heated along its boundary. We outline the fluid dynamics of this simple system and through the use of computational fluid dynamics (CFD), explain the mechanisms that give rise to a plethora of interesting properties, from a lensing action resulting in the focussing of light, to a simulator of optical turbulence in the laboratory. The CFD models are supported in most cases by intuitive analytical expressions, teasing out fundamental physics from the fluid dynamics of this system, while the predicted impact of the fluid dynamics on the optical field is verified experimentally. Despite the simplicity of the system – merely a spinning, heated pipe – the fluid dynamics of the system is shown to be rather complex, comprising regions of slow and fast flow, symmetric and asymmetric density gradients, and laminar and turbulence regions. We conclude the study by outlining how such aero-optics, using aerodynamics and fluid flow to control light, may be exploited in applications ranging from long range telescopes to overcoming the damage thresholds of conventional solid state glass optics for delivery of high power lasers.

2. Gas lenses

The principle of operation of the spinning, heated, pipe as a gas lens, an example of which is shown in Fig. 1, is based on the concept that the shear viscosity of air increases when heated, so that when the outside wall of the pipe is heated the layer of air next to the pipe's inner wall is heated as well. During rotation this inner layer is centrifugally expelled and replaced by cold air from the surroundings, inhaled along the axis from both ends, resulting in an axial (air) region that is cooler compared to the air at the wall. This temperature gradient creates a density gradient resulting in a refractive index gradient conducive to focusing, thus the name: gas lens. Rotating the heated pipe converts the density with a vertical gradient due to gravity to one that is rotationally symmetric about the axis. In order to customise the aero-optic for a lensing action, it is necessary to create a parabolic density gradient (and hence temperature gradient) across the pipe, and preferably everywhere along its length. A purely parabolic gradient in the density would be an ideal GRIN lens: the perfect gas lens.

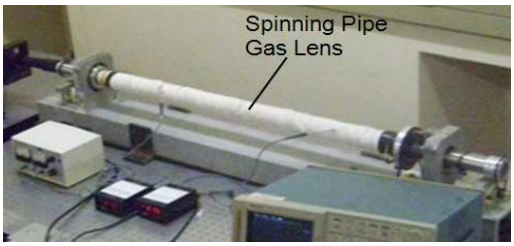

Fig. 1. An image of the spinning pipe gas lens (SPGL), comprising a steel pipe that is heated and spun around its axis. The central heated section is evident by the white heater tape surrounding it.

Previous studies have shown that the SPGL imitates a graded index (GRIN) medium with a refractive index which is a maximum along the axis and decreases parabolically with radial distance r, towards the walls (Michaelis, 1986; Forbes, 1997; Mafusire, 2006)

$$n(r) = n_0 - \tfrac{1}{2}\gamma^2 r^2 \tag{1}$$

The radial refractive index parameter, γ is a measure of the power of the SPGL, while n_o is the refractive index along the axis.

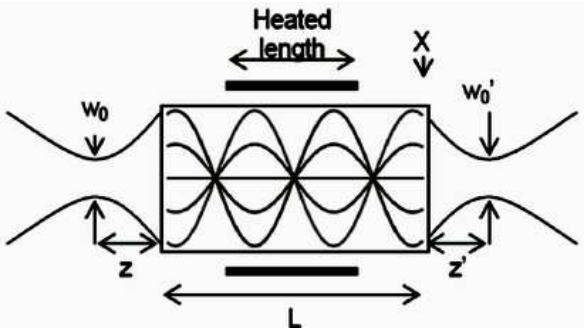

Fig. 2. A laser beam being converged on exit from a spinning pipe gas lens.

The focal length of the lens in terms of the input and output beam waist positions, w_0 and w_0', located at respective distances, z and z' with respect to the SPGL (Fig. 2) is given by (Mafusire, 2008b)

$$f = \frac{1}{2(z'-z)}\left[z_0^2 + \frac{1}{\gamma^2} + 2zz' - z \pm \sqrt{z_0^4 + 2z_0^2\left(\frac{1}{\gamma^2} + 2z' - z^2\right) + \left(\frac{1}{\gamma^2} + z^2\right)^2} \right] \tag{2}$$

where z_0 is the beam's Rayleigh range in front of the lens.

The earliest gas lenses were made at Bell Laboratories in an early attempt at producing waveguides for long range communication as a forerunner to the optical fibre. They were operated by heating the walls to a suitably high temperature then cold air was injected along the axis, creating a graded index between the lower density of the hot marginal air and increasing radially towards the cooler axis. Any laser beam propagating along the axis is refracted towards the denser axis hence were referred to as the tubular gas lenses. Early work was done by Berreman (Berreman, 1965) and Marcuse (Marcuse, 1965). In fact Marcuse showed that these lenses approximate a thin lens since both their principal planes coincide. Beyond the potential use for waveguiding (Kaiser, 1968), they were also used as telescope objectives (Aoki, 1967).

The main disadvantage with this design was that convection currents were clearly present and so introduced aberrations due to gravity on the laser beam wavefront. Gloge (Gloge, 1967) showed that the optical centre of such lenses is displaced vertically downwards, an effect which increased with tube diameter. Kaiser (Kaiser, 1970) circumvented this problem by designing a gas lens where hot gas could be exhausted radially, with the cold gas injected as before, resulting in improved performance. Meanwhile, in the former Soviet Union, another improvement was made by replacing the gas injection with rotating a heated pipe about its axis (Martynenko, 1975). It was demonstrated, theoretically and experimentally, that the rotation removed distortions due to gravity by creating a rotationally symmetric density distribution which completely overcame the convection currents of the tubular gas lens.

The investigation into this version of this gas lens design, now called the spinning pipe gas lens, or SPGL for short, was taken over by the then University of Natal without the knowledge of the research in the former USSR. They worked with a vertical lens which was used for focusing a high power laser for drilling holes into metal sheets (Michaelis, 1986). Another improvement was to combine both rotation and gas injection to create a steady focus (Notcutt, 1988). An interesting application was when the SPGL was used as a high quality telescope objective to take images of sun spots and moon craters, illustrating the power of such devices (Michaelis, 1991). Further improvements included operating the SPGL at pressures higher and lower than atmospheric pressure (Forbes, 1997) in order to control the focal length, and careful characterisation of the temperature distribution inside the pipe (Lisi, 1994).

Recently a more modern approach to understanding such devices has been completed, considering the interface of fluid dynamics with physical optics propagation and characterisation of laser beams (Mafusire et al, 2007; Mafusire et al, 2008a; Mafusire et al, 2008b; Mafusire et al, 2010a; Mafusire et al, 2010b). Using computational fluid dynamics (CFD) to simulate the density and velocity distributions inside the SPGL, one can deduce the phase change imparted to the light through the Gladstone-Dale law, thus making it possible

to calculate optical aberrations at any plane along the beam's path. To appreciate this, consider the gas medium where the density at each point in the medium fluctuates about a certain mean density, σ. These density fluctuations result in refractive index fluctuations also about a mean refractive index, N. These two parameters are related by the Gladstone-Dale law given by (Zhao et al, 2010)

$$N = G(\lambda)\sigma + 1 \tag{3}$$

where $G(\lambda) = 2.2244 \times 10^{-4}[1 + (6.7132 \times 10^{-8} / \lambda)^2]$, the wavelength dependant Gladstone -Dale constant which has a value of about 2.25 × 10^{-4} m^3/kg in air for HeNe laser radiation (λ = 6.328 × 10^{-7} m). If the geometrical length of the laser beam path in the gas lens is given by, l, then the phase change of the laser beam is given by

$$\phi = klN \tag{4}$$

where $k = 2\pi / \lambda$ is the laser beam wavenumber for radiation of wavelength, λ. The implication is that the optical distortions in the gas lens, due to imperfect control of the fluid to create the lens, can be measured by observing the phase changes in the laser beam. Distortions to the phase are called optical aberrations. The measurement of the optical aberrations of this particular aero-optic has introduced a very interesting paradox: rotation of the gas lens removes distortions due to gravity, but as we will see later, the other aberrations increase in magnitude as the rotation speed and the wall temperature increase. Therefore such optics are not perfect. To understand where the imperfections originate from, we start with a computational fluid dynamics (CFD) model of the gas lens.

2.1 Computational fluid dynamics model of the gas lens

To confirm the theoretical analysis of the SPGL given above and the optical aberrations measured from its performance, a computational fluid dynamics (CFD) simulation of a simplified test system was executed using the commercial CFD code, STAR–CD® using the $k-\varepsilon$ model which involves the numerical solution of two coupled equations, a turbulent kinetic energy (k) equation and an energy dissipation rate (ε) equation [Blazek, 2001; Davison, 2011]. The purpose of this study was to show the effect of the heat and mass transfer on the velocity distribution and density. Assumptions included the removal of the mounts and other three-dimensional geometry features that would complicate the geometric model. The pipe used in the model was based on the dimensions of the actual SPGL we have in the laboratory: 1.43 m in length and with an internal diameter of 0.0366 m. The heated section of the pipe was approximately 0.91 m long, leaving two unheated end lengths of length 0.25 m each. The pipe was accurately reproduced with the further assumption that the mounts act as a heat sink and thus the pipe ends are unheated. A fully transient solution is presented in which the pipe is spun up from a heated (at a temperature of 100 ^oC) steady-state buoyancy-driven solution, and held at fixed speed of 20 Hz until a steady state was reached.

The mesh used in the solution consisted of 350 transverse slices regularly arranged along the pipe's length. Each slice consisted of 512 nodes distributed across the section with more nodes concentrated along the boundary (see Fig. 3). The results extracted from the model included density for each data point in the centre of the cell in the mesh and animations

showing the evolution of the velocity and density at selected transverse and longitudinal cross-sections. Temperature distribution was extracted from the density data.

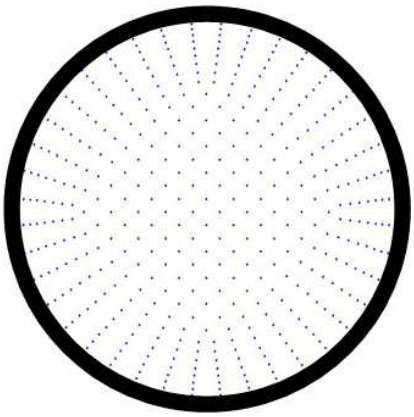

Fig. 3. The SPGL mesh transverse cross-section used in the CFD model.

2.1.1 Velocity distribution

Fig. 4 is a longitudinal cross-section of the gas lens showing the velocity distribution for various cuts of the pipe: (a) left third of the pipe, (b) the mid-section of the pipe, and (c) the right third of the pipe. The velocity distribution in the unheated sections is dominated by transverse movement of air towards the centre from both sides in the inviscid section

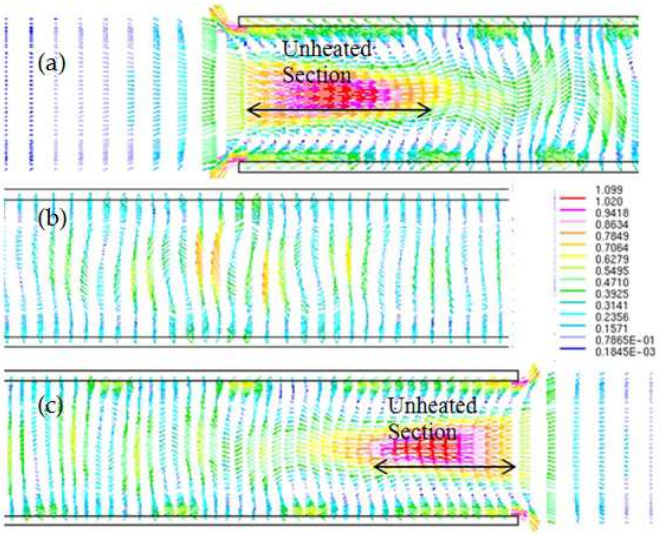

Fig. 4. Velocity profiles in the SPGL for the (a) left end section, (b) the mid-section of the pipe, and (c) the right end section.

outwards along the boundary section, with rotation playing very little or no part. As one moves towards the centre of the pipe length, the transverse speed of incoming air decays (as expected). In the boundary layer, the expelled air is fastest as it exits from the pipe. As the air along the boundary approaches the pipe end, it increases in both translation and rotational velocity, thus the boundary expels hot air in a spiral motion at both ends of the pipe. From this velocity distribution, we can infer the heat distribution in the inviscid region since fast moving air accumulates transversely injected heat much more slowly compared to stationary air. This means the incoming air is cooler but accumulates heat as it slows down and approaches the centre. This might point to a situation where the temperature along the axis at the centre is higher than that of the walls: because of the particles' slow velocity, they accumulate heat over time.

A closer look at the velocity profile of Fig. 4 (b) shows the complicated velocity distribution away from ends of the pipe. This could be evidence of multi-cellular flow, the irregularity of which is most likely responsible for the presence of some of the optical aberrations. This oscillatory activity is expected to increase with increase in wall temperature or rotation speed, which in turn, increases the magnitude of the optical aberrations.

2.1.2 Density distribution

The initial state of the gas in a heated stationary heated SPGL is a result of natural convection. A CFD simulation of this is shown in Fig. 5 (a): it shows a density gradient that decreases vertically so that at the gas is layered in horizontal bands within the pipe. When the pipe is spun the image changes radically: the vertical density gradient gives way to a density gradient that has rotational symmetry due to the forced convection of the rotating system, with the highest density along the axis and decreases towards the edges of the pipe (see Fig. 5 (b)). This is an example of a customised aero-optic: such a density distribution is conducive to focusing, since it results in a refractive index profile given by Eq. (1).

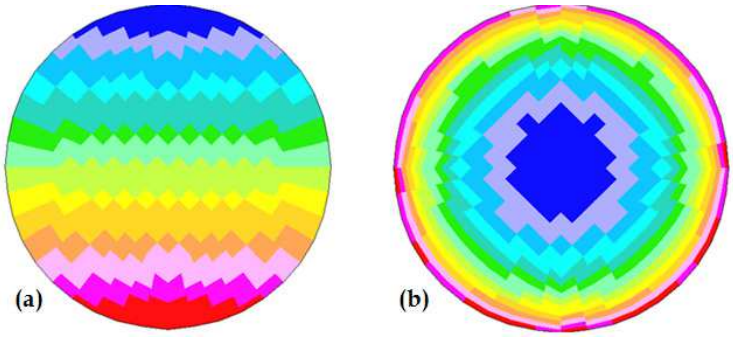

Fig. 5. Cross–sectional density profiles of an SPGL showing: (a) the initial state after heating, and (b) the rotating steady–state near the end face of the pipe, with high density centre (blue) and low density edges (red).

The other results from the density calculations confirm the velocity profile from the previous sub-section. The temperature (T) distribution was extracted from the density (ρ) data using the relation, $\rho = \rho_o(1 - a(T - T_o))$ where a = 2.263123×10^{-4} K^{-1} is the coefficient of volume expansion of air and ρ_o is the known density at a known temperature, T_o which we

take to be room temperature. Fig. 6 (a) shows a 3D plot of the density profile of the air everywhere along the length of the pipe for a particular (but arbitrary) cross-section. From this one can visualise the density distributions in transverse sections at critical planes, and a zoomed in view of the centre of the pipe is show in Fig. 6 (b). The corresponding temperature profile shows that the unheated section is at room temperature (27 ^{o}C) and the centre of the pipe is at about 100 ^{o}C, the temperature of the wall.
From Figs. 4 and 6 we can start to understand how this particular device works: the intake of cold and the expulsion of hot air, which takes place the ends of the pipe, results in parabolic-like density profiles near the pipe ends, which results in the lensing effect. As can be observed in the transverse profiles, a significant parabolic density distribution is only evident in a short section of the entire length, possibly less than half. As the pipe is spun faster, so this "lensing length" increases, making the lens stronger. A closer look at the cross-section profiles in Fig 6 (a) shows that some of them have a quartic density distribution, albeit for a very short length compared to the purely parabolic density profile, and this is the source of spherical aberration which has been shown to increase with rotation speed and/or temperature (Mafusire et al, 2008a).

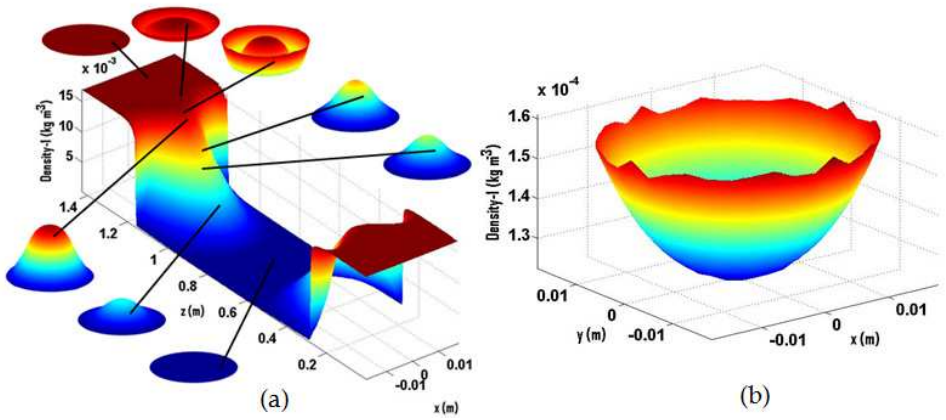

Fig. 6. (a) A 3D longitudinal density profile for the SPGL showing transverse sections at critical planes, and (b) the transverse density profile at the centre of the SPGL.

Another interesting observation from the CFD model of the SPGL is the transverse temperature profile in the centre of the pipe, i.e. away from the face ends, which reveals that the temperature along the axis is just over 0.16 K higher than at the walls, corresponding to a density 4×10^{-5} kg m^{-3} lower than at the walls (Fig 6 (b)). The explanation for this is that because air particles at this part of the pipe are moving very slowly and thus accumulates heat faster due to both convection and conduction. Thus, somewhat counter intuitively, the central heated part of the gas lens actually results in a decrease in the lensing action.

2.2 Experimental verification of the gas lensing

The experimental setup used is shown in Fig. 7. When the pipe is not rotated and not heated, no lensing takes place, and the phase of the light is taken as a reference. One expects

that if the pipe acts as a lens, the parabolic refractive index will result in curvature on the phase of the light, indicative of a lens. To test this, the pipe was heated to wall temperatures of 348 K, 373 K, 398 K and 423 K, and spun at various rotation speeds (limited to 20 Hz in our experiments). As the pipe is spun, so the focal length of the lens decreased, suggesting a stronger lens. Similarly, when the wall temperature of the pipe was increased, the lensing became stronger. Experimental results of this lensing is shown in Fig. 8.

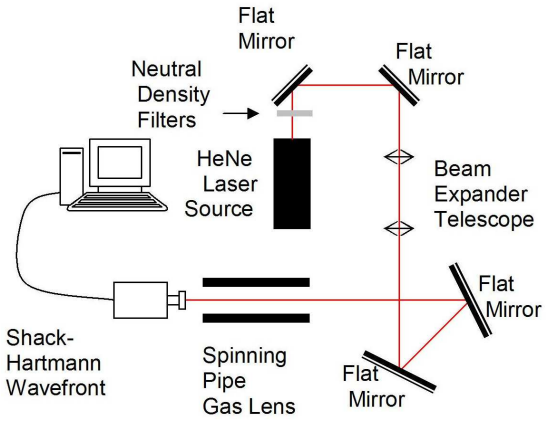

Fig. 7. Experimental setup used to test the lensing properties of the gas lens.

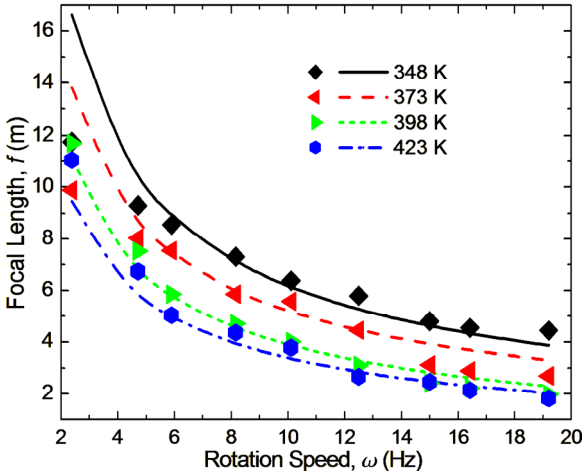

Fig. 8. The strength of the lensing action of the gas lens increases with both pipe rotation speed and pipe wall temperature. Short focal lengths suggest a strong lens, while long focal lengths suggest a weak lens.

3. Optical aberrations

We have seen earlier that the gas lens is aberrated due to the inability to completely control the fluid as desired. In order to describe just how aberrated the lens is, we introduce the concept of optical aberrations, and their description by Zernike polynomials, the coefficients of which are correlated to the magnitude of the optical aberrations. Once these coefficients are known, we can calculate the rms phase error (the deviation from flatness) and the Strehl ratio – how good the focus is for retaining power in a small spot.

3.1 Zernike polynomials

The phase of a laser beam can be written as a linear combination of Zernike polynomials. Zernike polynomials are unique in that they are the only polynomial system in cylindrical co-ordinates which are orthogonal over a unit circular aperture, invariant in form with respect to rotation of the co-ordinate system axis about the origin and include a polynomial for each set of radial and azimuthal orders [Born & Wolf, 1998; Dai, 2008; Mahajan, 1998; Mahajan, 2001]. More importantly, the coefficients of these polynomials can be directly related to the known aberrations of laser beams, making them invaluable in the description of phase errors. The transverse electric field of a laser beam, U, in cylindrical coordinates, ρ and θ can be represented by the product of the amplitude ψ and phase φ as shown by

$$U(\rho,\theta) = \psi(\rho)e^{i\varphi(\rho,\theta)} \tag{5}$$

The expansion of an arbitrary phase function, $\varphi(\rho,\theta)$, where $\rho \in [0,1]$ and $\theta \in [0, 2\pi]$, in an infinite series of these polynomials will be complete. The circle polynomials of Zernike have the form of an angular function modulated by a real radial polynomial. We can represent each Zernike term by

$$Z_{nm}(\rho,\theta) = C_{nm}R_{nm}(\rho)\Theta_m(\theta) \tag{6}$$

The angular part is defined as

$$\Theta_m(\theta) = \begin{cases} cosm\theta, & m > 0 \\ sinm\theta, & m < 0 \\ 1, & m = 0 \end{cases} \tag{7}$$

whereas the radial part is a polynomial given by

$$R_{nm}(\rho) = \sum_{k=0}^{\frac{n-m}{2}} \frac{(-1)^k (n-k)!\rho^{n-2k}}{k!(\frac{n+m}{2}-k)!(\frac{n-m}{2}-k)!} \tag{8}$$

where n and m are the non-negative order and ordinal numbers respectively which are related such that $m \le n$ and $n-m$ is even. C_{nm} is the respective coefficient for a particular aberration and can be either A_{nm} and B_{nm} depending whether the aberration is either even or odd, respectively.

This means that a laser beam wavefront described by a phase function φ can be expanded as a linear combination of an infinite number of Zernike polynomials, using generalized coefficients as follows

$$\varphi(\rho,\theta) = 2\pi\sum_{n=0}^{\infty} A_{n0}R_{n0}(\rho) + 2\pi\sum_{n=1}^{\infty}\sum_{m=1}^{n} R_{nm}(\rho)\left[A_{nm}cosm\theta + B_{nm}sinm\theta\right] \quad (9)$$

n	m						
	-3	-2	-1	0	1	2	3
0							
1							
2				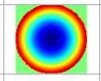			
3							
4							

Table 1. Contour plots of the Zernike primary aberration polynomials.

n	m	Description and symbol	Polynomial
0	0	Piston, A_{00}	1
1	-1	y-Tilt, B_{11}	$\sqrt{2}\rho\sin\theta$
	1	x-Tilt, A_{11}	$\sqrt{2}\rho cos\theta$
2	-2	y-Astigmatism, B_{22}	$\sqrt{6}\rho^2 sin2\theta$
	0	Defocus, A_{20}	$\sqrt{3}(2\rho^2-1)$
	2	x-Astigmatism, A_{22}	$\sqrt{6}\rho^2 cos2\theta$
3	-3	y-Triangular Astigmatism, B_{33}	$\sqrt{8}\rho^3 sin3\theta$
	-1	y-Primary Coma, B_{31}	$\sqrt{8}(3\rho^3-2\rho)sin\theta$
	1	x-Primary Coma, A_{31}	$\sqrt{8}(3\rho^3-2\rho)cos\theta$
	3	x-Triangular Astigmatism, A_{33}	$\sqrt{8}\rho^3 cos3\theta$
4	0	Spherical Aberration, A_{40}	$\sqrt{5}(6\rho^4-6\rho^2+1)$

Table 2. The names of the Zernike primary aberration coefficients.

The A and B terms are referred to as the symmetric and non-symmetric coefficients, respectively, in the units of waves. If the phase is known as a function, then the *rms* Zernike coefficients A_{nm} and B_{nm} can are calculated using

$$A_{nm} = \frac{1}{\pi}\sqrt{\frac{2(n+1)}{1+\delta_{m0}}}\int_0^{2\pi}\int_0^1 \varphi(\rho,\theta)R_{nm}(\rho)cosm\theta\rho d\rho\theta \quad (10a)$$

$$B_{nm} = \frac{1}{\pi}\sqrt{\frac{2(n+1)}{1+\delta_{m0}}}\int_0^{2\pi}\int_0^1 \varphi(\rho,\theta)R_{nm}(\rho)sinm\theta\rho d\rho\theta \tag{10b}$$

where δ_{m0} is the Kronecker delta function and the integrals' coefficients are normalizing constants. The names of the coefficients of primary aberrations which we are going to discuss in this paper are given in Table 1. From the aberration coefficients, we can calculate the wavefront error, the Strehl ratio (Mahajan, 2005), focal length (Mafusire and Forbes, 2011b) and the beam quality factor (Mafusire & Forbes, 2011a). The Strehl ratio is defined as the ratio of the maximum axial irradiance of an aberrated beam over that of a diffraction limited beam with the same aperture size. The general definition of the Strehl ratio is given by (Mahajan, 2001; Mahajan, 2005).

$$\begin{aligned} S &= \left(\frac{\left| \int_0^{2\pi}\int_0^1 \psi(\rho)e^{i\phi(\rho,\theta)}\rho d\rho d\theta \right|}{\int_0^{2\pi}\int_0^1 \psi(\rho)\rho d\rho d\theta} \right)^2 \\ &\approx e^{-(\Delta\varphi^2)} \end{aligned} \tag{11}$$

In the last result, we have used an approximation of the Strehl ratio for small aberrations less than the wavelength of the radiation. For a better undstanging on the wavefront error and Strehl ratio, the interested reader is referred to Mahajan (Mahajan, 2001; Mahajan, 2005).

3.2 Calculation of Zernike primary aberrations from CFD density data

A practical way to extract Zernike coefficients from CFD density data is to generate phase data in layers normal to the propagation direction of the beam using Eq. 4 with distance l between layers. A Taylor polynomial fit given by Eq. 12 is made to each plane to create a phase function in Cartesian form.

$$\begin{aligned} \varphi(x,y) = {} & p_{00} + p_{10}x + p_{01}y + p_{02}y^2 + p_{11}xy + p_{20}x^2 + p_{03}y^3 + p_{12}xy^2 + p_{21}x^2y \\ & + p_{30}x^3 + p_{04}y^4 + p_{13}xy^3 + p_{22}x^2y^2 + p_{31}x^3y + p_{40}x^4 + p_{05}y^5 + p_{14}xy^4 \\ & + p_{23}x^2y^3 + p_{32}x^3y^2 + p_{41}x^4y + p_{50}y^5 \end{aligned} \tag{12}$$

We can then convert the Cartesian coordinates to cylindrical coordinates using $x = rcos\theta$ and $y = rsin\theta$, replace r with ρ/a then reduce the resultant function. If we substitute this function into Eq. 10 we can then extract the *rms* primary Zernike coefficients which are given by Eq. 13. These equations enable us to calculate the Zernike coefficients from the phase distribution data. With these data, it is possible to work out the phase change experienced by the laser beam as it is propagates through each layer. If we have data for the next layer, and the one after that, then it is possible to work out the impact on the laser beam as the output from one layer becomes the input for the next layer. If the density of each layer is known from a CFD model, then propagating the laser beam through the medium in this manner will approximate the total aberrations imparted to the laser beam, assuming the propagation distance is small. In our simulations we have restricted our description of the aberrations to the fourth order, but of course one can make the expansion as accurately as one desires.

$$
\begin{aligned}
A_{00} &= \tfrac{1}{24}(a^2(a^2(3p_{04} + p_{22} + 3p_{40}) + 6p_{02} + 6p_{20}) + 24p_{00}) \\
A_{11} &= \tfrac{1}{96}\, a\,(a^2(3\,(a^2(p_{14} + p_{32} + 5p_{50}) + 8p_{30}) + 8p_{12}) + 48p_{10}) \\
B_{11} &= \tfrac{1}{96}\, a\,(a^2(3\,a^2(5p_{05} + p_{23} + p_{41}) + 24p_{03} + 8p_{21}) + 48p_{01}) \\
A_{20} &= \tfrac{1}{16\sqrt{3}}(a^2(a^2(3p_{04} + p_{22} + 3p_{40}) + 4p_{02} + 4p_{20})) \\
A_{22} &= \tfrac{1}{8\sqrt{6}}(a^2(-3a^2(p_{04} - p_{40}) - 4p_{02} + 4p_{20})) \\
B_{22} &= \tfrac{1}{16\sqrt{6}}(a^2(3a^2(p_{13} + p_{31}) + 8p_{11})) \\
A_{31} &= \tfrac{1}{120\sqrt{2}}(a^3(3\,(a^2(p_{14} + p_{32} + 5p_{50}) + 5p_{30}) + 5p_{12})) \\
B_{31} &= \tfrac{1}{120\sqrt{2}}(a^3(3a^2(5p_{05} + p_{23} + p_{41}) + 15p_{03} + 5p_{21})) \\
A_{33} &= -\tfrac{1}{40\sqrt{2}}((a^3(a^2(3p_{14} + p_{32} - 5p_{50}) + 5p_{12} - 5p_{30})) \\
B_{33} &= \tfrac{1}{40\sqrt{2}}(a^3(a^2(-5p_{05} + p_{23} + 3p_{41}) - 5p_{03} + 5p_{21})) \\
A_{40} &= \tfrac{1}{48\sqrt{5}}(a^4(3p_{04} + p_{22} + 3p_{40}))
\end{aligned}
\tag{13}
$$

3.3 Piston as a measure of average density

It is well known that piston is the average phase of a wavefront (Mahajan, 1998; Dai, 2008). In our formulation, Zernike coefficients are in the units of waves and phase is in radians, so that the piston is related to the average phase by $A_{00} = \frac{1}{2\pi}\bar{\varphi}$. Substituting for the phase as defined in Eq. 4 and introducing a new term, $L = l / \lambda$, the piston becomes $\bar{\varphi} = L\bar{N}$ where $\bar{N}$ is the average refractive index. Finally, combining these two equations and then substituting for the average refractive index as defined by Eq. 3, the result is

$$A_{00} = L(G\bar{\sigma} + 1) \tag{14}$$

The equation implies that the piston measured for a beam having passed through a medium of length, *l*, is directly proportional to average density in that medium. This means that if you have divided a propagation path of a laser beam in an aero-optic medium to steps each of length, *l*, then the variation of piston for each step is actually the variation in average density. This equation can also mean that if the piston is known after the beam has passed through such a medium, then we can use it to calculate the total average density of that path. If the density in the path is a constant, or $\sigma = \bar{\sigma}$, measuring piston can now be used to measure density. This would be true if all aberrations, except for piston, are zero, or at the very least, very small compared to piston. We can also conclude that the greater piston is compared to other aberrations, the more uniform the medium is.

3.4 Extraction of the optical parameters from the CFD model

Returning to our gas lens, CFD density data was extracted from 351 planes equally spaced along the length of the pipe, so that we model the pipe as 350 layers, or "individual gas lenses" placed one after another, each of length 4.1 mm. Density data is converted to refractive index data using the Gladstone-Dale's law and from this, the phase, φ is calculated using Eq. 4 with *l* set to 4.1 mm. A Taylor polynomial surface fit was carried out for each plane to create a phase function in Cartesian form. The coefficients thus acquired

were used to calculate the Zernike coefficients, using Eq. 13, resulting in 350 sets of primary Zernike coefficients for the spinning pipe gas lens. It is instructive to partition the SPGL data into sections based on the known fluid behaviour discussed earlier, as illustrated in Fig. 9. These are the end sections, labelled A, which are just over 20 cm each, the central section, C, of about 20 cm. This leaves the two sections in-between, B, each about 40 cm. Sections A are unheated. Let us assume that the laser beam is propagating through the pipe with its axis coinciding with that of the pipe. The beam should be small enough not to experience any diffraction with the pipe walls. For that reason we choose a, of size 0.371 cm against a pipe of radius 1.83 cm. The size of the beam was set at 0.548 cm, the same beam size we used as in the experiment (Mafusire, 2008a). We further assume that the only aberrations the beam experiences are from the medium and not from diffraction due to the propagation itself.

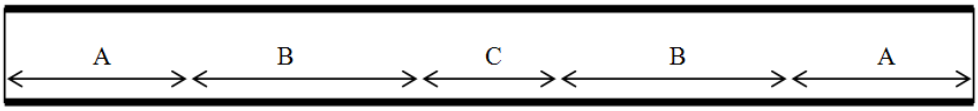

Fig. 9. Sections for analysing the spinning pipe gas lens based on the fluid behaviour disussed earlier.

We now present the graphs of all the primary aberrations as shown in Fig. 10. The aberrations have been organised starting with piston, followed by defocus, spherical aberration, tilt, coma and then astigmatic aberrations, i.e., astigmatism and triangular astigmatism (see Figure 10 (a)-(e)). Piston, Fig. 10 (a), has a characteristic curve which shows local average density, related to the overall phase delay experienced by the beam (Eq. 14). It is maximum in section A of the gas lens and minimum in section C. Section A is where the pipe is not heated and section C is the hot section where rotational motion is dominant. Section B is dominated by a phase gradient. This is the section in which the hot outgoing air mixes with the cool incoming air. We might call it the mixing length. This is the turbulent section of the pipe; the source of aberrations. At the same time, piston is much larger compared to other aberrations. Local piston has an average size of about 3.76 λ whereas the second most dominant one is defocus which has an average less than -0.005 λ, a factor of about 700. This implies that the density in each slice is almost uniform. From this, we can tell that the lens is very weak. Considering defocus, Fig. 10 (b), we notice immediately that focusing takes place in two parts of the pipe: the sections labelled B, with a large contribution from the region interfacing with section A, reaching a local maximum of -0.015 λ. Along its length, the SPGL has two centres of focus (sections B), thus making the SPGL very difficult to align. This confirms the 3D profile in Fig. 6 (a), that the lensing action of the SPGL comes from the mixing of hot and cold air.

The higher order aberrations increase dramatically in section B, suggesting that it is the mixing that gives rise to lensing also has a deleterious effect on the laser beam. This is because the mixing of hot and cold air creates local random varying density, which generates aberrations, the effect of which should increase with temperature and/or rotation speed. Spherical aberration reaches a local maximum of 0.0085 λ a magnitude half the size of defocus. Tilt also increases in the same region with a maximum of around 0.00002 λ. This behaviour is similar to the behaviour exhibited by coma (Fig. 10 (e)) though the values are about 10 times smaller.

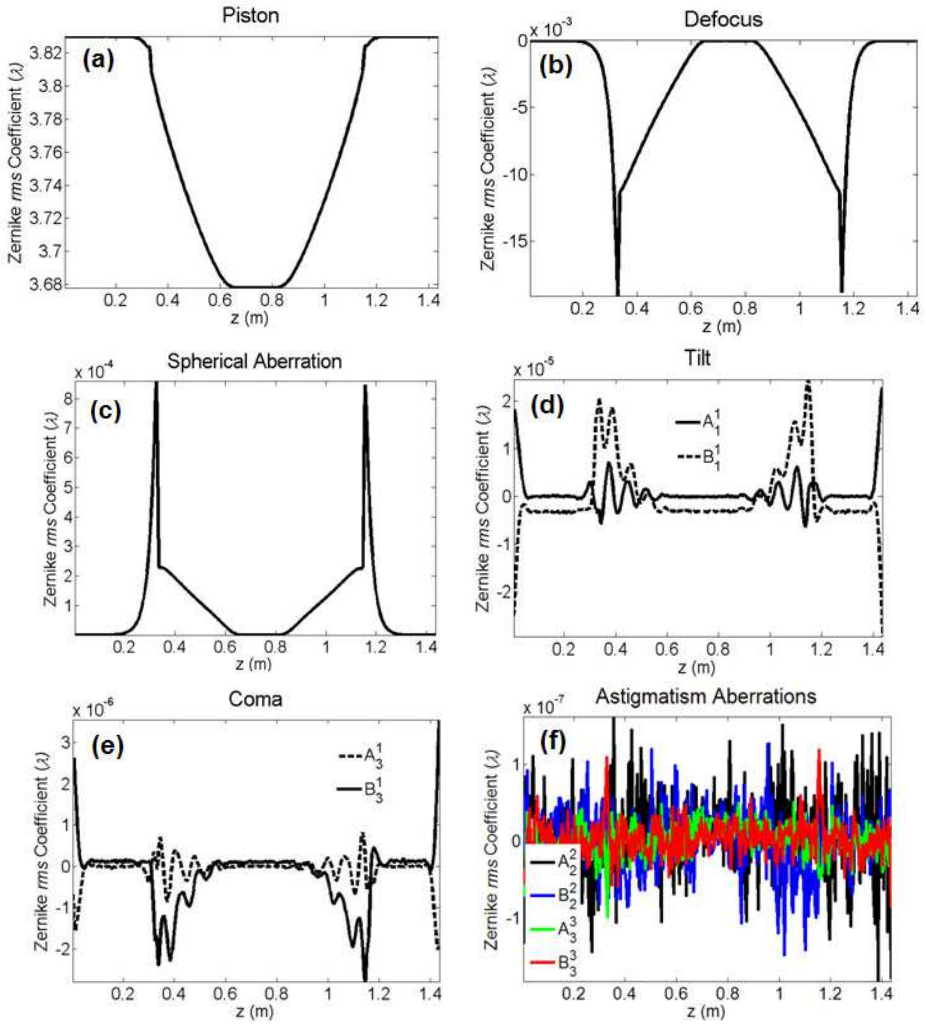

Fig. 10. Local optical aberration distribution along the SPGL calculated from the CFD density data

The beam quality factor distribution (Figure 11 (a)) in the SPGL confirms the aberration distribution. The beam quality factor is highest (suggesting a poor beam) at the same points where spherical aberration is highest. Of all the aberrations, spherical aberration has the largest coefficient. This confirms that spherical aberration is biggest contributor to beam quality deterioration in a gas lens. The wavefront error and Strehl ratio provide further proof of this. However, the important thing to note is that these parameters prove that the gas lens does not cause deterioration of the laser beam by that much. An unaberrated Gaussian beam has an M^2 of 1, whereas the model shows local values of M^2 of about 1.57. This results in a very low local wavefront error of about 0.0001 λ^2 on average. The Strehl ratio (Fig. 11b) is almost always 1 throughout the SPGL except in the mixing length where it

drops by an infinitesimally small amount. The overall beam quality factor for the entire gas lens was found to be 2.5071 in both axes. The only disappointing aspect of the lens was its focal length which was found to be 5.03 m in both axes. This confirms that the gas lens is a very weak lens.

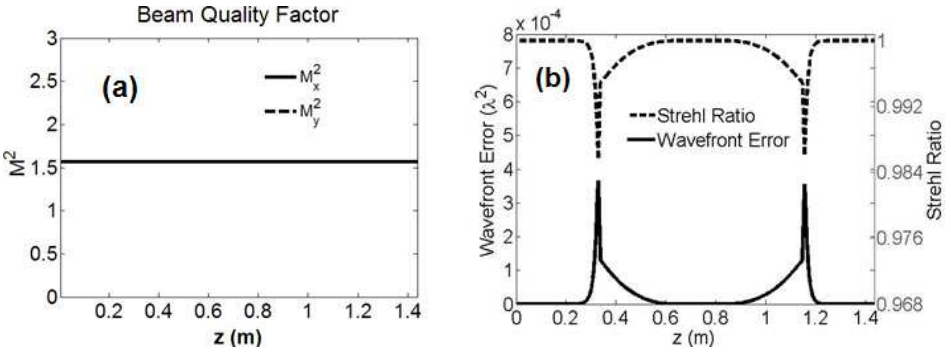

Fig. 11. The local beam quality factor (a), wavefront error and Strehl ratio (b) distributions along the pipe calculated from the SPGL CFD density data

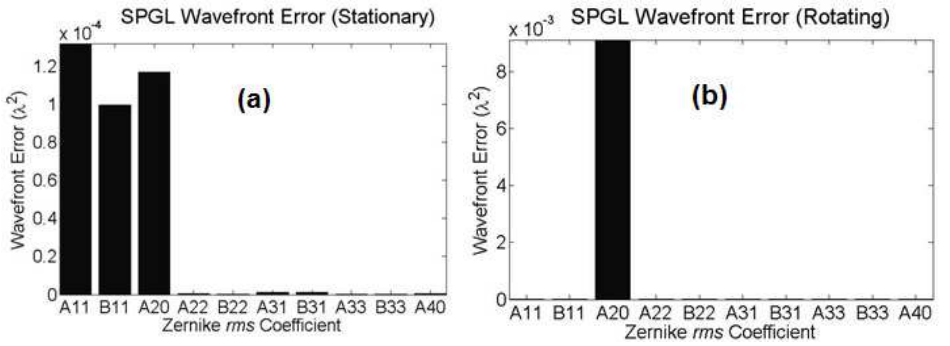

Fig. 12. Global primary optical aberrations except piston calculated from the SPGL CFD density data summarising the overall SPGL for a stationary (a) and rotating (b) heated pipe.

Now let us summarise the performance of the SPGL by looking at the CFD calculated global wavefront error for a heated stationary (Figure 12 (a)) and a rotating (Figure 12 (b)). The results for a stationary SPGL show the dominance of tilt in both axes, both with have values of at least 10^{-4} λ^2. Defocus has a value around the average of the two. This confirms that there is, indeed some focusing before rotation begins, though it is still very small, about 1.2×10^{-4} λ^2. However, as rotation commences, there is a significant increase in defocus, to 9.2×10^{-3} λ^2, which dominates other aberrations, including till, by a large amount. On the other hand, x- and y-tilt drop slightly from 1.3×10^{-4} λ^2 and 10^{-4} λ^2 to just below 10^{-5} λ^2. This confirms the fact that before rotation, the SPGL is dominated by tilt, due to gravitational distortion, but the effect is completely reduced under steady state rotation leaving defocus completely dominant. In other words, we have customised the density gradient to produce a lens.

3.5 Experimental verification of the SPGL model

Since density is directly proportional to refractive index, the phase of a laser beam propagating through a gas lens will be altered depending on the refractive index distribution. For completeness, we present a summary of the optical investigation on the aberrations generated by an actual SPGL that was characterised with a Shack-Hartmann wavefront sensor (Mafusire et al, 2008a). An expanded HeNe laser beam steered by flat mirrors is made to propagate through the lens. A Shack-Hartmann wavefront sensor was placed just behind the lens and used to measure the beam's quality and phase aberrations for rotation speeds up to about 17 Hz for wall temperatures 351, 373, 400 and 422 K.

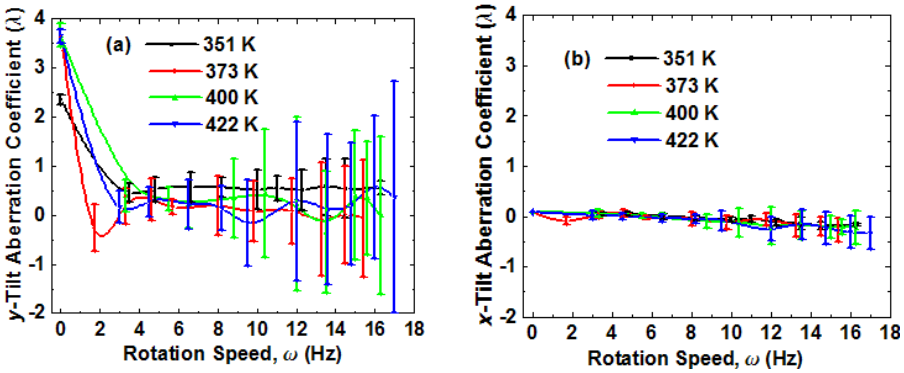

Fig. 13. y–Tilt (a) and x–tilt (b) generated by a spinning pipe gas lens at selected wall temperatures and rotation speeds.

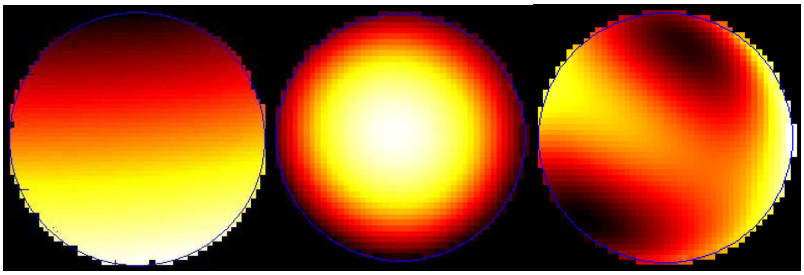

(a) (b) (c)

Fig. 14. The phase distribution of the laser beam with: (a) no rotation but heated to 422 K, showing tilt; (b) after rotating the SPGL at 17 Hz, showing significant curvature on the wavefront; and (c) same conditions as in (b) but with defocus and tilt removed, revealing the higher order aberrations.

The first result confirms the fact that rotation removes distortions which are caused by gravity: y-tilt, which is induced by gravity is reduced to a bare minimum as soon as rotation commences (Fig. 13 (a)) whereas x-tilt remains very small (Fig. 13 (b)) throughout. We can observe the same effect by looking the phase distribution before and during rotation. Figs. 14 (a) and (b) show the phase distribution before and during rotation, respectively. The phase maps are dominated by y-tilt (Fig. 14 (a)) before rotation, and defocus (Fig. 14 (b))

during rotation. However, digital removal of defocus and tilt reveals the presence of higher order aberrations, Fig. 14 (c). This phase map helps illustrate the other result observed during the experiment, the effect of the SPGL on the beam quality factor.

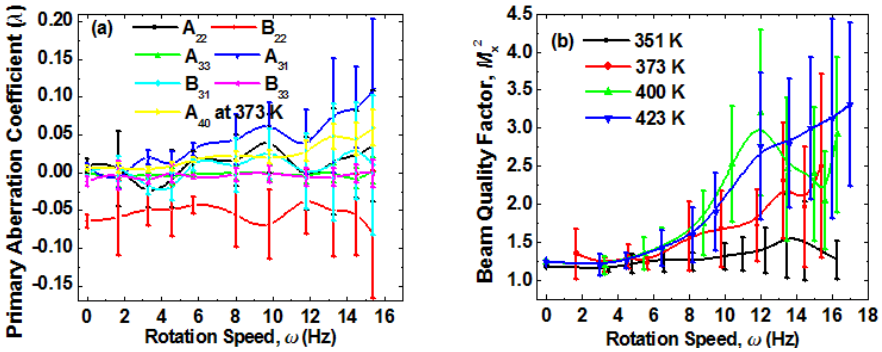

Fig. 15. (a) Higher order aberrations introduced by the SPGL; (b) increase in M_x^2 with rotation speed and temperature as a direct result of the aberrations in (a).

The other aberrations increase in magnitude as the rotation speed and/or wall temperature is increased (Fig. 15 (a)) thereby increasing the beam quality factor, M^2 (Fig. 15 (b)). This confirms the fact that the gas lens also generates aberrations which are increasing in power as the lens becomes stronger.

4. Optical turbulence

We now ask if the SPGL may be used as a controlled turbulence medium in the laboratory for the study of the propagation of optical fields through the atmosphere. The basis of this question is the fact that the SPGL introduces aberrations, and further that these aberrations may be controlled through the rotation speed and temperature of the pipe. Optical turbulence may also be described by aberrations, except that the weighting of the aberrations should take on a particular form. Characterising the aberrations in the SPGL from a turbulence perspective shows that the turbulence is uniform and isotropic near the pipe axis (about which it is spun), becoming non-uniform and anisotropic at the pipe boundary. A modified von Karman turbulence model (Andrews & Phillips, 2005) is used to analyse the turbulence strength along the pipe axis, and we find that the turbulence strength increases with rotation speed and pipe-wall temperature allowing for 'controlled' turbulence in the laboratory: our simple system allows for a controlled adjustment of the refractive index structure constant by more than two orders of magnitude.

The results of Fig. 16 illustrate this: in Fig. 16 (a) the log of the structure constant, which is a measure of the turbulence strength, is adjusted by two orders of magnitude as the pipe parameters of rotation speed and wall temperature are adjusted. Other supporting data (not shown here) confirms that the aberration weighting is correct for a particular atmospheric turbulence model – the modified von Karman turbulence model. This model has an inner and outer scale, the smallest and largest scales of the turbulence in the atmosphere respectively, relating directly to the smallest and largest fluid flow structures. These parameters can be measured in the pipe, and are shown in Fig. 16 (b). The pertinent point is that all the characteristics of the turbulence can be measured and therefore simulated in this simple aero-optic device, allowing for easy experiments of atmospheric turbulence in the laboratory.

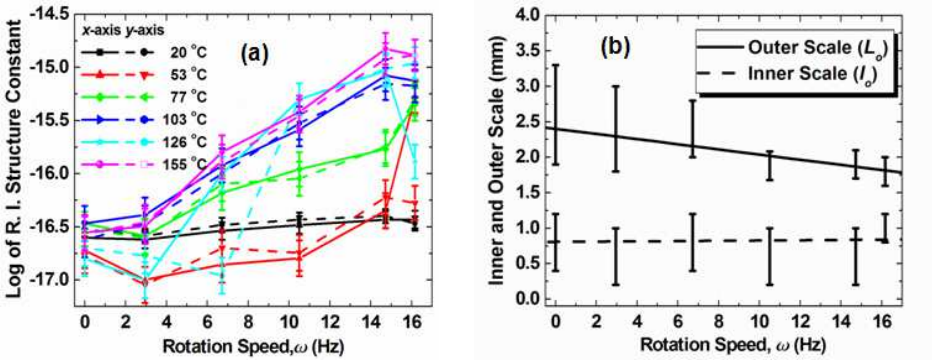

Fig. 16. (a) Refractive index structure constant at selected rotation speeds and wall temperature. (b) Inner and outer scales at the selected rotation speeds. These are standard parameters used to describe optical turbulence, and illustrate that our aero-optic may be used as a simulator of turbulence.

We also consider the optical aberrations imparted to the field when propagating near the boundary layer (Fig. 17), and find the phase distortions to the laser beam to be dominated by *x*-astigmatism with *y*-astigmatism and tilt, increasing dramatically in magnitude at the highest rotation speed and temperature. It is apparent that, in the spinning pipe gas lens, the parent flow is derived from the rotation of the pipe.
It is this rotation, together with the physical size of the lens, which limit the outer scale of the turbulence in the pipe. On the other hand, the outer scale is not much larger than the inner scale for a small inertial sub range, the range of scales between which the turbulence is isotropic, homogenous and independent of the parent flow.

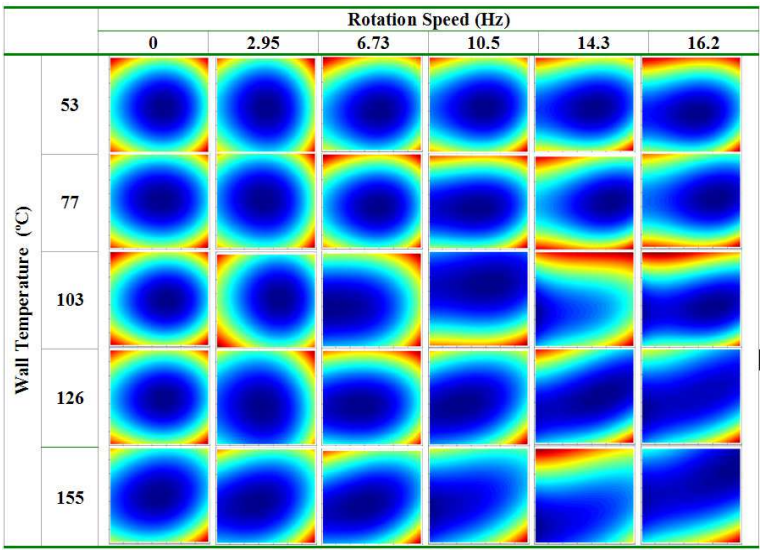

Fig. 17. Phase maps of the beam as it propagates near the boundary layer of the flow, for various wall temperatures and rotation speeds.

5. Summary

Aero-optics has found some novel applications of late, recently reviewed by Michaelis et al (Michaelis et al, 2006). These include long range telescoping elements, replacing high power laser windows to overcome damage threshold problems, adaptive lenses for delivery of high power laser beams in space propulsion experiments, and potential applications in laser fusion, control of peta-watt laser beams, photo-lithography with virtual capillaries and possibly novel guiding media for laser accelerators. Certainly if the quality of gas lenses could be improved, then the virtually limitless damage threshold of such lenses would make them ideal for most high power laser applications. The only drawback of most aero-optical devices is the distortions introduced to the laser beam due to imperfect control of the fluid, but as we have shown here, even this property may be exploited to simulate atmospheric turbulence in the laboratory.

In this chapter we have shown that it is possible to control the fluid flow inside a spinning heated pipe such that the density gradient of the air inside the pipe acts as a lens. As the focal length of this lens is a function of the rotation speed of the pipe and the temperature of the pipe wall, one has a variable focal length lens. We have shown focal lengths from infinity down to a couple of meters. We have shown that the lens is unfortunately aberrated, but highlighted that such aberrations un fact match atmospheric turbulence, so that the system may also be used as a simulator of atmospheric turbulence in the laboratory – again in a controlled and adjustable manner. It is this property – that such devices may be controlled – that makes aero-optics such an attractive possibility for future optical devices.

6. Acknowledgment

We would like to thank M.M. Michaelis for significant advice and for providing the original motivation for studying this field, and G. Snedden for his invaluable assistance in executing the CFD commercial code.

7. References

Andrews, L. C. & Phillips, R. L. (2005). *Laser Beam Propagation through Random Media*, SPIE Press.

Aoki, Y. & Suzuki, M. (1967). Imaging Property of a Gas Lens", *IEEE Trans. on Microwave Theory & Techniques*, Vol. 15, No. 1.

Blazek, J., (2001). *Computational Fluid Dynamics - Principles and Applications, Ch 7* Elvesier, Oxford.

Berreman, D. W., (1965). Convective Gas Light Guides or Lens Trains for Optical Beam Transmission, *J. Opt. Soc. Am*, Vol. 55, No. 3, pp. 239-247.

Born, M. & Wolf, E. (1998). *Principles of Optics: Electromagnetic theory of propagation, interference and diffraction of light 7th Ed* Cambridge University Press, Cambridge 517-553.

Dai, G-m, (2008). *Wavefront Optics for Vision Correction*, SPIE Press.

Davison, L., (2011). An Introduction to Turbulence Models. *Chalmers University of Technology*. Available from the University of Chalmers website: www.tfd.chalmers.se/~lada/postscript_files/kompendium_turb.pdf

Forbes, A. (1997). *Photothermal Refraction and Focusing*, PhD Thesis, University of Natal, Durban, South Africa.

Gloge, D. (1967). Deformation of Gas Lenses by Gravity, *Bell Sys. Tech. J.*, Vol. 46, No. 2, 357–365.

Kaiser, P. (1967). Measured Beam Deformations in a Guide Made of Tubular Gas Lenses, *Bell Sys. Tech. J.,* Vol. 47, 179–194.

Kaiser, P. (January, 1970). An improved thermal gas lens for optical beam waveguides, *Bell Sys, Tech. J.* Vol. 49, (January 1970) pp 137-153

Kellet, B.J.; Griffin, D.K.; Bingham R.; Campbell R.N.; Forbes, A. & Michaelis, M.M. (2008). Space polypropulsion, *Proc. SPIE* Vol. 7005, pp. 70052W-1.

Lisi, N.; Bucellato, R. & Michaelis, M. M. (1994). Optical quality and temperature profile of a spinning pipe gas lens, *Optics and Laser Technology,* Vol. 26, 25–27.

Mahajan, V. N., (1998). *Optical Imaging and Aberrations, Part I: Ray Geometrical Optics*, SPIE Press.

Mahajan, V. N. (2001). *Imaging and Aberrations, Part 2: Wave Diffraction Optics*, SPIE Press.

Mahajan, V. N., (2005). Strehl ratio of a Gaussian beam, *J. Opt. Soc. Am. A* Vol. 22, No. 9.

Martynenko, O. G., (1975). Aerothemooptics, *International J. of Heat and Mass Transfer.* 18, 793–796.

Michaelis, M. M.; Notcutt, M. & Cunningham, P. F. (1986). Drilling by a Gas Lens Focused Laser, *Opt. Comm*. Vol. 59, 369–374.

Michaelis, M. M.; Dempers, C. A.; Kosch, A. M.; Prause, A.; Notcutt M.; Cunningham, P. F. & Waltham, J., (1991). Gas lens telescopy, *Nature* Vol.353, 547-548.

Michaelis, M.M.; Forbes, A.; Conti, A.; Nativel, N.; Bencherif, H.; Bingham, R.; Kellett, B. & Govender, K. (2006). Non-solid, non-rigid optics for high power laser systems, *Proc. SPIE* Vol. 6261, pp. 15.1–15.13.

Mafusire, C. (2006). *Gas Lensing in a Heated Rotating Pipe*, MSc Thesis, University of Zimbabwe, (2006).

Mafusire, C.; Forbes, A.; Michaelis, M. M. & Snedden, G. (2007). Characterization of a spinning pipe gas lens using a Shack-Hartmann wavefront sensor", *Laser Beam Shaping VIII, Ed. F. Dickey, Proc. SPIE.*, Vol. 6663, 6663H.

Mafusire, C.; Forbes, A.; Michaelis, M. M. & Snedden, G. (2008a) Optical aberrations in a spinning pipe gas lens", *Opt. Exp.,* Vol. 16, No. 13, 9850-9856.

Mafusire, C.; Forbes, A.; Michaelis, M. M. & Snedden, G. (2008b). Spinning pipe gas lens revisited, SA. J. Sc., Vol. 104.

Mafusire, C.; Forbes A.; Michaelis M.M. & Snedden, G. (2010a). Optical aberrations in gas lenses, *Proc. SPIE* 7789, pp. 778908-1.

Mafusire, C., Forbes, A. & Snedden, G. (2010b). A computational fluid dynamics model of a spinning pipe gas lens, *Proc. SPIE* 7789, pp. 77890Y-1.

Mafusire, C. & Forbes, A., (2011a). The Beam Quality Factor of Truncated Aberrated Gaussian Laser Beams, *J. Opt. Soc. Am. A,* Vol. 28, No. 7, 1372-1378.

Mafusire, C. & Forbes, A., (2011b). The Mean Focal Length of an Aberrated Lens, *J. Opt. Soc. Am. A* Vol. 28, No. 7, 1403-1409 (2011).

Mafusire, C. & Forbes, A., (2011c) Controlling optical turbulence in the laboratory, Appl. Opt. (submitted for publication).

Marcuse, D. (1965). Theory of a Thermal Gradient Gas Lens, *IEEE Trans. on Microwave Theory & Technology,* Vol. MMT-13, No. 6, 734–739 (1965).

Notcutt, M; Michaelis, M. M.; Cunningham, P. F. & Waltham, J. A. (1988). Spinning Pipe Gas Lens, *Optics and Laser Technology,* 20(5), 243–250.

Siegman, A. E. (1999). Laser Beams and Resonators: The 1960s, *IEEE Jour. of special topics in Quant. Elec.* Vol. 20, No. 5, 100–108.

Steier, W. H. (1965) Measurements on a Thermal Gradient Gas Lens, *IEEE Trans. on Microwave Theory & Technology,* Vol. MMT-13, No. 6, 740–748.

Zhao, Y. X., Yi, S. H., Tian, L. F., He, L & Cheng, Z. Y., (2010) An experimental study of aero-optical aberration and dithering of supersonic mixing layer via BOS, *Science China: Physics, Mechanics & Astronomy* Vol. 53, No. 1, 89-94.

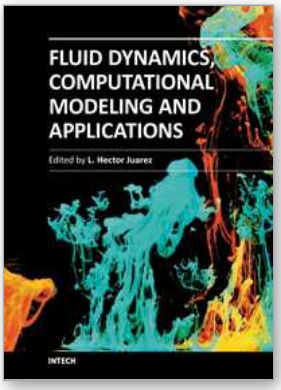

Fluid Dynamics, Computational Modeling and Applications

Edited by Dr. L. Hector Juarez

ISBN 978-953-51-0052-2
Hard cover, 660 pages
Publisher InTech
Published online 24, February, 2012
Published in print edition February, 2012

The content of this book covers several up-to-date topics in fluid dynamics, computational modeling and its applications, and it is intended to serve as a general reference for scientists, engineers, and graduate students. The book is comprised of 30 chapters divided into 5 parts, which include: winds, building and risk prevention; multiphase flow, structures and gases; heat transfer, combustion and energy; medical and biomechanical applications; and other important themes. This book also provides a comprehensive overview of computational fluid dynamics and applications, without excluding experimental and theoretical aspects.

InTech Europe
University Campus STeP Ri
Slavka Krautzeka 83/A
51000 Rijeka, Croatia
Phone: +385 (51) 770 447
Fax: +385 (51) 686 166
www.intechopen.com

InTech China
Unit 405, Office Block, Hotel Equatorial Shanghai
No.65, Yan An Road (West), Shanghai, 200040, China
中国上海市延安西路65号上海国际贵都大饭店办公楼405单元
Phone: +86-21-62489820
Fax: +86-21-62489821